The Astrophysical Journal, 837:145 (12pp), 2017 March 10 https://doi.org/10.3847/1538-4357/837/2/145
© 2017. The American Astronomical Society. All rights reserved.

The X-Ray and Mid-infrared Luminosities in Luminous Type 1 Quasars

Chien-Ting J. Chen(陳建廷)[1,2], Ryan C. Hickox[2], Andrew D. Goulding[3], Daniel Stern[4], Roberto Assef[5], Christopher S. Kochanek[6], Michael J. I. Brown[7], Chris M. Harrison[8], Kevin N. Hainline[2,9], Stacey Alberts[9], David M. Alexander[8], Mark Brodwin[10], Agnese Del Moro[11], William R. Forman[12], Varoujan Gorjian[4], Christine Jones[12], Stephen S. Murray[12], Alexandra Pope[13], and Emmanouel Rovilos[8]

[1] Department of Astronomy and Astrophysics, Pennsylvania State University, University Park, PA 16802, USA; ctchen@psu.edu
[2] Department of Physics and Astronomy, Dartmouth College, 6127 Wilder Laboratory, Hanover, NH 03755, USA
[3] Princeton University, Department of Astrophysical Sciences, Ivy Lane, Princeton, NJ 08544, USA
[4] Jet Propulsion Laboratory, California Institute of Technology, 4800 Oak Grove Dr., Pasadena, CA 91109, USA
[5] Núcleo de Astronomía de la Facultad de Ingeniería, Universidad Diego Portales, Av. Ejército Libertador 441, Santiago, Chile
[6] Department of Astronomy, Ohio State University, 140 West 18th Avenue, Columbus, OH 43210, USA
[7] School of Physics, Monash University, Clayton 3800, Victoria, Australia
[8] Centre for Extragalactic Astronomy, Department of Physics, Durham University, South Road, Durham, DH1 3LE, UK
[9] Steward Observatory, University of Arizona, Tucson, AZ 85721, USA
[10] University of Missouri, 5110 Rockhill Road, Kansas City, MO 64110, USA
[11] Max-Planck-Institut für Extraterrestrische Physik (MPE), Postfach 1312, D-85741, Garching, Germany
[12] Harvard-Smithsonian Center for Astrophysics, 60 Garden Street, Cambridge, MA 02138, USA
[13] Department of Astronomy, University of Massachusetts, Amherst, MA 01003, USA
Received 2016 August 29; revised 2017 January 5; accepted 2017 January 17; published 2017 March 13

Abstract

Several recent studies have reported different intrinsic correlations between the active galactic nucleus (AGN) mid-IR luminosity ($L_{\rm MIR}$) and the rest-frame 2–10 keV luminosity ($L_{\rm X}$) for luminous quasars. To understand the origin of the difference in the observed $L_{\rm X}$–$L_{\rm MIR}$ relations, we study a sample of 3247 spectroscopically confirmed type 1 AGNs collected from Boötes, *XMM*-COSMOS, *XMM*-XXL-North, and the Sloan Digital Sky Survey quasars in the *Swift*/XRT footprint spanning over four orders of magnitude in luminosity. We carefully examine how different observational constraints impact the observed $L_{\rm X}$–$L_{\rm MIR}$ relations, including the inclusion of X-ray-nondetected objects, possible X-ray absorption in type 1 AGNs, X-ray flux limits, and star formation contamination. We find that the primary factor driving the different $L_{\rm X}$–$L_{\rm MIR}$ relations reported in the literature is the X-ray flux limits for different studies. When taking these effects into account, we find that the X-ray luminosity and mid-IR luminosity (measured at rest-frame 6 μm, or $L_{6\,\mu\rm m}$) of our sample of type 1 AGNs follow a bilinear relation in the log–log plane: $\log L_{\rm X} = (0.84 \pm 0.03) \times \log L_{6\,\mu\rm m}/10^{45}\,{\rm erg\,s^{-1}} + (44.60 \pm 0.01)$ for $L_{6\,\mu\rm m} < 10^{44.79}\,{\rm erg\,s^{-1}}$, and $\log L_{\rm X} = (0.40 \pm 0.03) \times \log L_{6\,\mu\rm m}/10^{45}\,{\rm erg\,s^{-1}} + (44.51 \pm 0.01)$ for $L_{6\,\mu\rm m} \geqslant 10^{44.79}\,{\rm erg\,s^{-1}}$. This suggests that the luminous type 1 quasars have a shallower $L_{\rm X}$–$L_{6\,\mu\rm m}$ correlation than the approximately linear relations found in local Seyfert galaxies. This result is consistent with previous studies reporting a luminosity-dependent $L_{\rm X}$–$L_{\rm MIR}$ relation and implies that assuming a linear $L_{\rm X}$–$L_{6\,\mu\rm m}$ relation to infer the neutral gas column density for X-ray absorption might overestimate the column densities in luminous quasars.

Key words: galaxies: active

1. Introduction

X-ray emission and mid-IR emission are both excellent tracers of supermassive black hole (SMBH) accretion activities. Since active galactic nucleus (AGN) emission at these wavelengths is less susceptible to the presence of obscuring material compared to optical wavelengths (e.g., Corrales et al. 2016), studying the correlation between the X-ray and mid-IR luminosities of AGNs is crucial for understanding the dust-enshrouded phase of galaxy–SMBH coevolution (e.g., Di Matteo et al. 2005; Hopkins et al. 2006; Gilli et al. 2007; Somerville et al. 2008; Treister et al. 2009). There are now a range of studies examining the correlation between AGN X-ray and mid-IR luminosities. (e.g., Lutz et al. 2004, Gandhi et al. 2009, Goulding et al. 2011, Krumpe et al. 2015, Stern 2015). Some of these works found that the mid-IR ($L_{\rm MIR}$) and X-ray luminosities ($L_{\rm X}$) follow an almost linear relation in low-redshift, low-luminosity AGNs (e.g., Lutz et al. 2004; Alexander et al. 2008; Gandhi et al. 2009; Lusso et al. 2011; Asmus et al. 2015). However, it is not clear whether such a linear relation holds for more luminous AGNs (i.e., quasars[14]). Notably, studies comparing $L_{\rm X}$ to the UV luminosity for AGNs found that the ratio between the X-ray and UV luminosities rapidly decreases with increasing UV luminosity for type 1 AGNs (e.g., Tananbaum et al. 1979; Strateva et al. 2005; Lusso et al. 2010). Since the rest-frame mid-IR emission of AGNs originates from the hot dust heated by the UV photons from the SMBH accretion disk, understanding the $L_{\rm X}$–$L_{\rm MIR}$ relation for luminous AGNs is also crucial for understanding the structure of the hot dust surrounding the central SMBH, as well as the AGN accretion physics.

The local, linear $L_{\rm X}$–$L_{\rm MIR}$ relation is illustrated by the results of Gandhi et al. (2009), who found that the spatially resolved nuclear $L_{\rm MIR}$ and $L_{\rm X}$ for local Seyfert galaxies are almost linearly correlated. Recently, Asmus et al. (2015) have extended this work to a number of more luminous AGNs from the 9-month *Swift*/BAT catalog (Tueller et al. 2008) and archival local AGNs with high spatial resolution mid-IR observations (Asmus et al. 2014).

[14] We refer to AGNs with bolometric luminosity ($L_{\rm bol}$) more luminous than 10^{45} erg s^{-1} as "quasars."

Asmus et al. (2015) found that the luminous AGNs in their sample have slightly more X-ray emission than the value predicted by the local linear relation between $L_{\rm MIR}$ and $L_{\rm X}$. While their result was only suggestive due to the limited size of their sample, it is supported by the study of higher-redshift AGNs selected from the Bright Ultra-hard *XMM-Newton* survey (Mateos et al. 2015). However, some studies have also reported a luminosity-dependent $L_{\rm X}$–$L_{\rm MIR}$ relation for luminous quasars, including the study of high-redshift AGNs in COSMOS by Fiore et al. (2009) and the compilation of Sloan Digital Sky Survey (SDSS) DR5 AGNs spanning a wide luminosity range studied by Stern (2015).

The lack of consensus on the universality of the $L_{\rm X}$–$L_{\rm MIR}$ correlations might be due to various observational limitations. In particular, for surveys such as COSMOS, the limited survey volumes restrict the number of rare AGNs detected at the highest luminosities. On the other hand, wide-area surveys have shallower flux limits, making them less likely to detect fainter sources and higher-redshift sources. Thus, the $L_{\rm X}$–$L_{\rm MIR}$ correlations could also be biased if the X-ray-nondetected objects are not taken into account.

To understand whether such biases might affect the observed $L_{\rm X}$–$L_{\rm MIR}$ relations, we compile four different type 1 AGN samples spanning a wide range of survey areas and X-ray flux limits to investigate the intrinsic relationship between AGN mid-IR and X-ray emission over a wide dynamic range in luminosity.

To minimize the contamination from star-formation-related processes and the stellar emission in the host galaxy, we focus on luminous objects that are spectroscopically confirmed as type 1 AGNs. We use type 1 AGN samples from the AGN and Galaxy Evolution Survey (AGES; Kochanek et al. 2012) in the Boötes survey region, the publicly available AGN samples from the *XMM*-COSMOS survey (Lusso et al. 2010), the *XMM*-XXL-North survey (Liu et al. 2016; Menzel et al. 2016; Pierre et al. 2016), and the SDSS DR5 quasars with serendipitous *Swift*/XRT observations (Wu et al. 2012a).

This paper is organized as follows. In Section 2 we describe the multiwavelength data and the properties of each quasar catalog. In Section 3 we discuss the derivations of X-ray and mid-IR luminosities. In Sections 4 and 5 we discuss the $L_{\rm X}$–$L_{6\,\mu\rm m}$ correlation and the possible biases that might affect the observed relations. A discussion and a summary are given in Section 6. Throughout the paper, we use the Vega magnitude system and assume a ΛCDM cosmology with $\Omega_m = 0.3$, $\Omega_\Lambda = 0.7$, and $H_0 = 70\,{\rm km\,s^{-1}\,Mpc^{-1}}$.

2. The Type 1 Quasar Samples

To investigate the correlation between X-ray luminosities and the mid-IR luminosities for type 1 AGNs with broad optical emission lines, we focus on extragalactic survey regions with X-ray observations and mid-IR observations from *Spitzer* or *WISE*. We select four different samples with a wide range of survey area and flux limits in order to understand the biases that might affect the observed $L_{\rm X}$–$L_{\rm MIR}$ relation.

2.1. Boötes Type 1 Quasar Sample

One primary source of quasars for this study is the Boötes multiwavelength survey, which has a wide area (9 deg^2) and excellent multiwavelength coverage. For this work, we use the 1443 AGNs in the AGES catalog that are classified as "type 1" based on spectroscopic observations from the Hectospec instrument on the MMT observatory (i.e., sources that are best fitted by the SDSS quasar template; see Kochanek et al. 2012, for details).

To ensure that the AGNs studied in this work have minimal impact from the radio-loud quasars that could have X-ray emission enhanced by the presence of relativistic jets (e.g., Zamorani et al. 1981; Wilkes & Elvis 1987; Cappi et al. 1996; Brinkmann et al. 2000), we also use the Westerbork Synthesis Radio Telescope (WSRT) observations of the Boötes region to eliminate powerful radio AGNs. De Vries et al. (2002) surveyed the central ≈7 deg^2 of the NDWFS field at 1.4 GHz to a limiting flux of ≈0.1 mJy and a beam size of 13″ × 27″. For the 46 matches (within 2″) between the WSRT radio sources and the AGES AGN catalog, we calculate their "radio-loudness" using a radio-loud definition of $R \geqslant 10$ (Kellermann et al. 1989). Radio-loudness is defined as the ratio between the 5 GHz and optical *B*-band (rest-frame) monochromatic luminosities, $R = L_{5\,\rm GHz}/L_B$. $L_{5\,\rm GHz}$ is derived from the WSRT observations at 1.4 GHz assuming a typical power-law spectrum, $S_\nu \propto \nu^{-0.7}$. The rest-frame L_B is derived using the spectral energy distribution (SED) fitting results described in Section 3.2. Of the 46 WSRT-detected sources, 33 of them are radio-loud AGNs ($R > 10$, Kellermann et al. 1989). We exclude the 33 radio-loud sources and focus on the remaining 1410 radio-quiet AGNs in the following analysis.

Boötes is also covered by the XBoötes survey, a 9.3 deg^2 mosaic of 126 short (5 ks) *Chandra* ACIS-I images (Kenter et al. 2005; Murray et al. 2005) covering the entire AGES field. XBoötes contains 2724 X-ray point sources with at least four counts in the AGES survey region. Of those, 790 X-ray point sources are far from bright stars and matched within 3.″5 to the 1410 type 1 AGNs with good spectroscopic redshifts from AGES at $0.14 < z < 3.61$ (Kenter et al. 2005; Hickox et al. 2009), yielding an X-ray detection fraction of ∼56% for the type 1 AGNs. These X-ray point sources have 0.5–7 keV luminosities of $10^{42}\,{\rm erg\,s^{-1}} < L_{\rm X} < 10^{45}\,{\rm erg\,s^{-1}}$, which are characteristic of moderate to luminous AGNs.

We also make use of the optical to near-IR broadband photometry available in the Boötes field, which includes optical photometry from the NOAO Deep Wide Field Survey (*Bw*, *R*, *I*; Jannuzi & Dey 1999), near-IR NEWFIRM (*J*, *H*, K_s; Gonzalez et al. 2010), mid-IR SDWFS (*Spitzer* IRAC; Ashby et al. 2009), and mid-IR observation at 24 μm from *Spitzer* MIPS (Rieke et al. 2004). An extensive description of the multiband photometry extraction can be found in Brown et al. (2007) and Chung et al. (2014).

Another advantage of the Boötes survey region is that it is covered by the Herschel Multi-tiered Extragalactic Survey (HerMES; Oliver et al. 2012). The inclusion of the far-IR photometry makes it possible to constrain the star formation rate even for luminous quasars (e.g., Netzer et al. 2007; Kirkpatrick et al. 2012; Mullaney et al. 2012; Chen et al. 2015), thus allowing for more accurate measurements of mid-IR AGN luminosities that could be contaminated by star formation processes. For this work, we adopt the SPIRE 250 μm photometry from Alberts et al. (2013). For the 1410 type 1 AGNs in AGES, ≈15% of them are detected by SPIRE at 250 μm. For these far-IR-detected AGNs, we carefully examine the resulting SED fits in Section 3.2 and their $L_{\rm X}$–$L_{\rm MIR}$ relation in Section 5.4.

2.2. XMM-COSMOS X-Ray AGN Sample

Since XBoötes is a relatively shallow X-ray survey, we supplement it with the publicly available *XMM*-COSMOS catalog of X-ray-selected type 1 AGNs from Lusso et al. (2010). The Lusso et al. (2010) catalog contains 545 X-ray AGNs, of which 322 have secure spectroscopic redshift measurements and broad emission line width $>2000\,\mathrm{km\,s^{-1}}$. The 322 type 1 AGNs in the *XMM*-COSMOS sample were selected from a parent sample of 361 type 1 AGNs by excluding the 39 radio-loud AGNs identified using the same radio-loudness definition as described in Section 2.1.

As discussed in Section 3.2, we utilize broadband multi-wavelength photometry to determine the AGN contribution to the mid-IR luminosity of our AGNs. To this end, we also make use of the publicly available broadband photometry in the COSMOS survey region culled from Capak et al. (2007), Sanders et al. (2007), and Elvis et al. (2012). In detail, we first obtain the optical positions by cross-correlating the *XMM*-COSMOS identification numbers (XIDs) of the Lusso et al. (2010) sources with those in the *XMM*-COSMOS multi-wavelength catalog (Brusa et al. 2010), in which the optical-to-X-ray counterpart association is obtained based on a likelihood-ratio technique (see Section 3 of Brusa et al. 2010, for details). We than cross-correlate the optical positions of the Lusso et al. (2010) sources to the Capak et al. (2007) and Sanders et al. (2007) catalogs. We use the broadband photometry spanning optical to far-IR wavelengths that are comparable to the Boötes survey region for the SED fits. In detail, we use the *Subaru* optical photometry at u, g, r, i, and z bands and the near-IR J, H, K from Calar Alto, UH 88", and Canada–France–Hawaii Telescope observatories, respectively. The mid-IR photometry comes from both the *Spitzer* IRAC and MIPS instruments, including 3.6, 4.5, 5.8, 8.0, 24, 70, and 160 μm. Similar to Boötes, the COSMOS survey region is also covered by HerMES. Therefore, we also match the *Herschel* SPIRE photometry to the 322 *XMM*-COSMOS AGNs with a 5″ search radius. The detection fraction at SPIRE 250 μm for the 322 XMM-COSMOS type 1 AGNs is also ∼15%. The L_{MIR} measurements and L_{X}–L_{MIR} relation of these far-IR-detected AGNs are also discussed in more detail in Sections 3.2 and in 5.4.

2.3. XRT-SDSS: Optical AGNs from SDSS and Swift/XRT

To investigate the L_{X}–L_{MIR} relation, it is also important to consider the possible biases created by missing the most luminous sources as a result of the limited volume of surveys like Boötes and *XMM*-COSMOS. For this purpose we use the *Swift*/SDSS catalog from Wu et al. (2012a, hereafter W12).

W12 matched all of the 77,429 optically selected SDSS DR5 quasars (Adelman-McCarthy & Collaboration 2007; Schneider et al. 2007) to the *Swift*/XRT archive (Burrows et al. 2005) and found that there are 1034 SDSS DR5 quasars within 20′ of a *Swift* pointing. We refer to this catalog as the XRT-SDSS catalog throughout the rest of the paper. Due to the serendipitous nature of the XRT-SDSS catalog, the *Swift*/XRT exposure time ranges from 1 to 600 ks. We follow the approach of W12 by focusing only on the 607 objects that are unambiguously identified as quasars and excluded objects that are radio-loud or obscured (see Table 9 of W12). W12 define a "clean sample" of quasars by enforcing a minimum XRT exposure time of >10 ks, which includes 241 objects with an 82% X-ray detection rate. To maximize the sample size, we also consider a more liberal exposure time cut at >5 ks. The 5 ks XRT-SDSS sample includes 362 objects with a 70% X-ray detection rate.

We also make use of the photometry from the SDSS DR5 quasar catalog by cross-matching the SDSSID from Table 7 of W12 to the SDSSID of the SDSS DR5 quasar catalog. All the quasars in the 10 and 5 ks samples have photometry in the u, g, r, i, and z bands, and ≈18% of the W12 quasars have Two Micron All Sky Survey (2MASS) J, H, and K_s photometry.

To estimate the AGN mid-IR luminosity, we match the SDSS DR5 coordinates to the ALLWISE catalog using a matching radius of 2″. We check the number of possibly misidentified sources by randomly shifting the positions of the XRT-SDSS sources by 1′ and matching the shifted positions to the ALLWISE catalog. We find that 1.5% of the randomly shifted positions have a *WISE* counterpart within 2″, suggesting that the spurious matching rate between the XRT-SDSS sources and the *WISE* catalog is about 1.5%, which has a negligible effect on the L_{X}–L_{MIR} relation. For the XRT-SDSS type 1 AGNs in the 10 and 5 ks samples, all of them have detections in at least three *WISE* bands.

2.4. XMM-XXL-North X-Ray AGN Sample

The *XMM*-XXL-North survey (hereafter XXL-N) is the northern part of the *XMM*-XXL survey, which is composed of two separate ∼25 deg^2 fields (Pierre et al. 2016). As part of the SDSS-III survey, X-ray sources matched to SDSS photometric objects with $r < 22.5$ in XXL-N were all targeted by SDSS-III's Baryon Oscillation Spectroscopic Survey (BOSS; Smee et al. 2013). The spectroscopic and photometric properties of the X-ray AGNs in XXL-N have recently been reported in Menzel et al. (2016, hereafter M16). Of the 3042 sources in the M16 catalog with BOSS spectra, 1787 are classified as "broad-line" AGNs based on the presence of broad emission lines (Hβ, Mg II, C III, or C IV) with FWHM larger than $1000\,\mathrm{km\,s^{-1}}$.

For this work, we directly use the SDSS photometry and *WISE* photometry provided by M16. The optical and mid-IR photometry in M16 is obtained by cross-matching the *XMM* positions with the SDSS or *WISE* positions using a likelihood-ratio matching method (see Georgakakis & Nandra 2011; M16, for details). To maximize the photometric coverage of this data set, we also obtain 2MASS photometry from the ALLWISE catalog, which provides the associations between the *WISE* source and the closest 2MASS source within a 3″ radius.

Notably, the M16 catalog includes X-ray sources from the XXL survey (Pierre et al. 2016), as well as the sources from the predecessor of XXL, the *XMM*-LSS survey. The *XMM*-LSS survey is a ≈4.5 deg^2 field at the center of XXL-N with deeper *XMM-Newton* coverage (10–40 ks). For this work, we consider only the sources with 0.5–2 keV fluxes above the "completeness limit" of the XXL survey, $5.0 \times 10^{-15}\,\mathrm{erg\,s^{-1}}$. This flux limit is equivalent to $\approx 1.1 \times 10^{-14}\,\mathrm{erg\,s^{-1}\,cm^{-2}}$ in the 0.5–7 keV band assuming a $\Gamma = 1.8$ X-ray power-law spectrum. With this flux limit, the number of broad-line AGNs is reduced to 1372. This approach also ensures that the XXL-N type 1 AGNs studied in this work have uniform X-ray coverage and high mid-IR detection fractions in the *WISE* bands (∼87% for 3.4, 4.6, and 12 μm bands).

We also match the XXL-N type 1 AGNs to the VLA FIRST catalog (Becker et al. 1995) with a 2″ radius. We calculate the radio-loudness of the 41 sources with FIRST counterparts using

Table 1
Survey Properties

Parameter	Boötes	*XMM*-COSMOS	XRT-SDSS (10 ks)	XRT-SDSS (5 ks)	XXL-North
X-ray survey area	9.3 deg^2	2.0 deg^2	…[a]	…	25 deg^2
No. of type 1 AGNs	1410	322	241	362	1153
z	0.14–4.58	0.10–4.25	0.08–3.68	…	0.06–5.0
$\langle m_r \rangle$	21.0	21.5	19.0	19.0	20.7
X-ray energy range (keV)	0.5–7 (*Chandra*)	0.5–10 (*XMM-Newton*)	0.3–10 (*Swift*/XRT)	…	0.5–10 (*XMM-Newton*)
0.5–7 keV X-ray flux limit (10^{-15} erg s^{-1} cm^{-2})	7.8	1.0	25.0	50.0	11.1
X-ray detection fraction	56%	100%	83%	70%	100%
Median L_X (2–10 keV) (log erg s^{-1})	44.23	44.15	44.66	44.66	44.26

Notes. The flux limits of *XMM*-COSMOS and the XRT-SDSS catalogs have been converted to 0.5–7 keV assuming a $\Gamma = 1.8$ power-law SED and Galactic extinction.
[a] The true survey area of the XRT-SDSS catalog is not well constrained owing to the varying X-ray exposure time of the catalog.
[b] The magnitude limit for target selection of XXL-N is based on r-band photometry.

the same approaches described in previous subsections. Of the 41 sources with FIRST counterparts, 38 of them satisfy the same "radio-loud" definition and are excluded. Since our goal is to study the relation between X-ray and mid-IR luminosities of type 1 quasars, we focus only on the 1153 X-ray-detected type 1 AGNs that are not radio-loud and have a $>5\sigma$ detection significance in at least three *WISE* bands.

2.5. Key Properties of Samples

We list the key properties of the samples used in this work in Table 1. A common feature of the sources selected from these four catalogs is that the sources are all optically confirmed as broad-line AGNs, which ensures that our L_X–L_{MIR} measurements should have a minimal impact due to obscuration. The median r-band magnitudes of these samples are 21.0, 21.5, 19.0, and 20.7 mag for AGES, *XMM*-COSMOS, *Swift*-SDSS, and XXL-N, respectively.

Both the AGES and *XMM*-COSMOS catalogs have heterogeneous spectroscopic depths. AGES specifically targeted sources identified as an AGN at other wavelengths down to $i < 22.5$, while for other galaxies the limiting magnitude is $i < 20$ (see Kochanek et al. 2012, for details). For the *XMM*-COSMOS sample, the spectroscopic data come from existing SDSS spectra, the magnitude-limited zCOSMOS catalog ($i < 22.5$, Lilly et al. 2009), and spectroscopic observations with MMT and IMACS/*Magellan* down to $i \approx 25$. For the SDSS DR5 quasar catalog, the spectroscopic depth is brighter ($i \lesssim 19.1$ for low-redshift quasars and $i < 20.2$ for higher-redshift quasars, see Schneider et al. 2007, for details). As for the XXL-N X-ray AGN catalog, the spectroscopic depth of BOSS is $r < 22.5$, which is deeper than the SDSS DR5 quasar catalog and similar to Boötes and *XMM*-COSMOS.

For the Boötes and XRT-SDSS samples, the mid-IR observations are from either *Spitzer* or *WISE* and are complete for these optically luminous AGNs;[15] thus, these samples are only flux limited in the optical and X-ray bands. Notably, the X-ray-nondetected objects in the AGES and XRT-SDSS samples are still covered by X-ray observations, which allows us to take the X-ray-nondetected sources into account when measuring the L_X–L_{MIR} relation. Both the *XMM*-COSMOS and XXL-N samples are X-ray selected, so these catalogs are flux limited in the X-ray and optical wavelengths. As for mid-IR observations, the *Spitzer* observations are complete for the *XMM*-COSMOS sample, and the *WISE* coverage for the XXL-N sample is also highly complete (~87%).

[15] Only for the three shorter-wavelength *WISE* bands.

3. Luminosities in the X-Ray and Mid-IR

In this section, we briefly describe the methods used to calculate the rest-frame 2–10 keV luminosity and the mid-IR luminosity for the AGNs in each catalog. For comparison, we plot the redshift, X-ray luminosity at rest-frame 2–10 keV (L_X), and luminosity of the AGN component at 6 μm ($L_{6\,\mu m}$) in Figure 1. The L_X and $L_{6\,\mu m}$ histograms are also shown in Figure 1.

3.1. X-Ray Luminosity

For the Boötes sample, the X-ray photon count rates in the 0.5–7 keV band are converted to a flux using a conversion factor of 7.8×10^{-15} erg cm^{-2} s^{-1} for an object with 4 counts in a 5 ks exposure. This is derived based on the assumption of an unabsorbed X-ray spectrum with a photon index of $\Gamma = 1.8$ (see Kenter et al. 2005; Murray et al. 2005, for a complete discussion). We then converted the 0.5–7 keV luminosity to the rest-frame 2–10 keV luminosity with a k-correction using the same spectral index. We note that Galactic absorption column density for the XBoötes survey is negligible ($\approx 10^{20}$ cm^{-2}), but we still take it into account in our calculation for consistency with other samples.

For the *XMM*-COSMOS sample, the rest-frame 2–10 keV X-ray luminosity comes from Lusso et al. (2010), in which the X-ray count rates in the 0.5–2 keV and 2–10 keV bands are converted into rest-frame 2–10 keV luminosities using a Galactic column density $N_H = 2.5 \times 10^{20}$ cm^{-2} (see Cappelluti et al. 2009), and assuming photon indices of $\Gamma = 2$ and $\Gamma = 1.7$ for the soft and hard bands, respectively. For consistency, we revise the 2–10 keV X-ray luminosities using the same approach and assumptions as applied to the XBoötes sample. This causes changes of ~8% relative to the values in Lusso et al. (2010) owing to the different assumptions regarding the intrinsic photon index of the X-ray power-law spectrum.

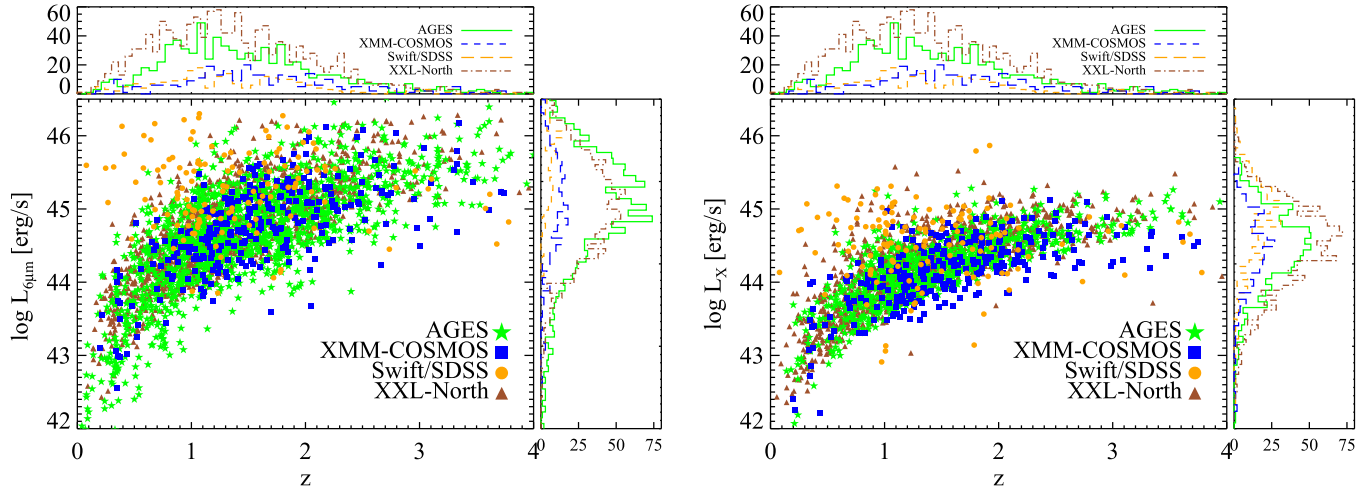

Figure 1. Redshift distributions of $L_{6\,\mu m}$ and L_X for different samples studied in this work. This figure shows that our samples span a wide range of X-ray and mid-IR luminosities, which is crucial for studying the intrinsic L_X–L_{MIR} relation of AGNs. The histograms of mid-IR and X-ray luminosities for the different samples are shown in the top panels on the left and right, respectively.

For the XRT-SDSS sample, the estimate of X-ray luminosity varies depending on the quality of available X-ray data. We briefly describe the approach taken by W12 and refer the readers to Section 2 in Wu et al. (2012a) for details. In the XRT-SDSS sample, the observed-frame 0.3–10 keV flux for each source with XRT counts >100 is derived by fitting the observed counts to estimate the X-ray power-law index and intrinsic absorption. For sources with between 30 and 100 XRT counts, the intrinsic absorption is fixed to zero while the spectral index is still a free parameter. For sources with XRT counts less than 30, the flux is obtained by assuming a fixed spectral index of $\Gamma = 2$ and a fixed zero intrinsic absorption. For consistency, we again modify the derived 2–10 keV L_X for the XRT-SDSS sample to account for the different choices in the AGN intrinsic spectral index. This causes changes of ∼15% relative to the values reported in W12.

For the XXL-N sample, the X-ray luminosities come from Liu et al. (2016), who estimated the *intrinsic* X-ray luminosity by jointly fitting the *XMM-Newton* PN and MOS data with the Bayesian X-ray Analysis package (BXA; Buchner et al. 2014).[16] The model used to fit the data is a combination of three different models that take the intrinsic power-law continuum, absorption, Compton scattering features, and a soft scattering component into account (see Section 4.1 of Liu et al. 2016, for details). To broadly assess whether the BXA-based L_X are comparable to our other estimates of L_X, we recalculate the X-ray luminosities for the XXL-N sample by converting the 0.5–8 keV photon count rates reported in Liu et al. (2016) to rest-frame 2–10 keV L_X assuming a power-law X-ray spectrum with a $\Gamma = 1.8$ photon index. The average difference from the BXA estimates is only 0.03 dex. This is not surprising, as type 1 X-ray AGNs have been found to have little to no absorption (e.g., Hickox et al. 2007). For this work, we adopt the BXA-based intrinsic L_X to minimize the possible bias on the measured L_X–L_{MIR} relation due to any X-ray absorption.

For the majority of type 1 quasars in AGES, *XMM-COSMOS*, and XRT-SDSS samples, the X-ray absorption correction to the X-ray luminosity is not available from spectral fitting owing to the limited photon counts. Therefore, the uncertainties in their X-ray luminosities were estimated based on Poisson noises of the count rates calculated using the Gehrels (1986) method. For these luminous type 1 AGNs, the intrinsic X-ray absorption could be considered negligible. In particular, an X-ray stacking analysis has shown that the hardness ratios for type 1 AGNs in Boötes are consistent with little to no absorption ($N_H \sim 10^{20}$ cm^{-2}; Hickox et al. 2007). We discuss the possible effects of X-ray absorption on the observed L_X–$L_{6\,\mu m}$ relation further in Section 5.2.

3.2. SED Fitting Analysis and Mid-IR Luminosity

To estimate the contamination from the host galaxy to the AGN mid-IR luminosity, we use SED fits to calculate the intrinsic, de-absorbed AGN mid-IR luminosity, including *Herschel* far-IR photometry when available.

We follow the approach described in Chen et al. (2015) by fitting the photometry with three different components: an AGN spanning from near-UV to far-IR, a stellar population in the host galaxy, and a model for dust emission from reprocessed starlight.

We created ad hoc AGN templates by combining the near-UV to near-IR empirical AGN template from Assef et al. (2010) with the infrared AGN SEDs from Mullaney et al. (2011) and Netzer et al. (2007). For each AGN template, we create a grid of AGN templates with $0 < E(B-V) < 10$ using a hybrid extinction curve combining an SMC-like (Small Magellanic Cloud) extinction curve at $\lambda < 3300$ Å (Gordon & Clayton 1998) with a Galactic extinction curve at longer wavelengths (Cardelli et al. 1989), with $R_V = 3.1$ for both (see Assef et al. 2010, for details).

For the host galaxy templates, we consider two different components: the contribution from the stellar population of the galaxy, which accounts for the optical to near-IR emission; and a starburst component, which represents the mid- to far-IR dust emission from reprocessed stellar light. For the stellar population component, we adopt the three empirical galaxy templates from Assef et al. (2010) representing starburst (Im), continuous star-forming (Sbc), and old stars (elliptical), respectively. We follow the approach described in Chen et al. (2015) by replacing the >4.9 μm hot dust components of the Sbc and Im templates assuming a Rayleigh–Jeans tail identical to the elliptical galaxy to create empirical stellar population templates without dust

[16] We note that one of the 1153 AGNs is only detected at the 0.5–2 keV band. For this object we calculate its 2–10 keV L_X based on the 0.5–2 keV flux assuming a power-law X-ray spectrum with a $\Gamma = 1.8$ photon index.

emission. For the starburst component, we use a total of 171 starburst templates from Chary & Elbaz (2001), Dale & Helou (2002), and Kirkpatrick et al. (2012) to accommodate a wide range of spectral shapes of star-forming galaxies.

Given the SED templates, we fit the observed photometry using a χ^2 minimization algorithm to find the best-fit SED for each object. From the best-fit SEDs, we calculate the monochromatic luminosities of the AGN component at 6 μm. To account for uncertainties in the derived $L_{6\,\mu\mathrm{m}}$ due to both the uncertainties in the flux measurements and any degeneracy between the AGN and host galaxy components, we employ a bootstrapping approach. For each source, we randomly scatter the original photometry in every band with their 1σ uncertainties and redo the SED fits. We repeat this process 500 times for each source. For the Boötes, *XMM*-COSMOS, XRT-SDSS, and XXL-N samples, the median $L_{6\,\mu\mathrm{m}}$ uncertainties are 0.08, 0.11, 0.12, and 0.13 dex, respectively.

For type 1 AGNs in our sample, the majority of the sources have mid-IR SEDs dominated by the AGN component. The average AGN fractions (the absorbed AGN component contribution at 6 μm) for the Boötes *XMM*-COSMOS and XRT-SDSS samples are 89%, 95%, 92%, and 81%, respectively. For 98% of the AGNs in our final sample, the AGN component dominates (AGN fraction >50%) at 6 μm. However, there is a caveat when estimating the host galaxy contamination at mid-IR wavelengths with the SED fitting approach for the XRT-SDSS sample. Unlike the Boötes and the *XMM*-COSMOS samples that include far-IR observations, the XRT-SDSS sample relies on a very small number of *WISE* photometric data points to constrain the host galaxy contribution in the mid-IR. Since starburst activity can also produce strong mid-IR emission, we use the 228 far-IR-detected sources in Boötes and *XMM*-COSMOS to examine whether the exclusion of far-IR photometry could affect the observed AGN 6 μm luminosity. We redid the SED fits excluding the photometry at observed wavelengths longer than 24 μm and then compared the estimates for $L_{6\,\mu\mathrm{m}}$. We found a median difference of only $\pm$0.03 dex, which is not surprising since the AGNs studied in this work are luminous optical quasars. This 0.03 dex uncertainty was added in quadrature to the measured $L_{6\,\mu\mathrm{m}}$ for all objects lacking far-IR photometry.

4. The Correlation between X-Ray and Mid-IR Luminosities for X-Ray-detected Quasars

In Figure 2, we show the L_X–$L_{6\,\mu\mathrm{m}}$ distributions of sources with X-ray detections for all four catalogs. For comparison, we also show the Gandhi et al. (2009), Mateos et al. (2015),[17] and Stern (2015) samples, along with the L_X–$L_{6\,\mu\mathrm{m}}$ relation for local Seyfert galaxies from Gandhi et al. (2009). Clearly, the four catalogs studied in this work show an L_X–$L_{6\,\mu\mathrm{m}}$ distribution departing from the Gandhi et al. (2009) relation and other roughly linear relations suggested by studies of local active galaxies (e.g., Lutz et al. 2004; Maiolino et al. 2007; Asmus et al. 2015). The L_X–L_6 μm distributions for our samples are in broad agreement with the Fiore et al. (2009) and Stern (2015) luminosity-dependent L_X–$L_{6\,\mu\mathrm{m}}$ relations for luminous X-ray AGNs. We have converted the monochromatic luminosities measured at different wavelengths for these comparison samples (e.g., 5.8 and 12 μm) to $L_{6\,\mu\mathrm{m}}$ using the Assef et al. (2010) AGN template.

[17] We note that for the five most X-ray-luminous quasars in this sample, one of them is a lensed quasar and three of them are radio-loud. Therefore, we do not include these objects in this plot.

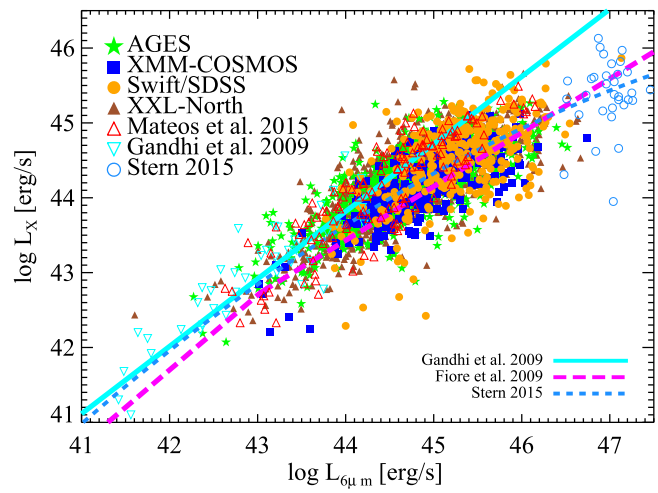

Figure 2. L_X–L_6 μm distribution for the four samples studied in this work. For comparison, the type 1 AGN sample from Mateos et al. (2015), the Seyfert galaxies from Gandhi et al. (2009), and the high-luminosity SDSS quasars from Stern (2015) and Just et al. (2007) are also shown. The approximately linear relation from Gandhi et al. (2009), the luminosity-dependent relation from Fiore et al. (2009), and the luminosity-dependent relation from Stern (2015) are shown as the solid line, long-dashed line, and short-dashed line, respectively. The luminous AGNs in our samples have systematically lower X-ray luminosities than predicted by the extension of the linear relation found for local Seyfert galaxies.

To obtain a simple parameterized L_X–$L_{6\,\mu\mathrm{m}}$ relation for AGNs spanning a wide range of AGN luminosity, we fit the combined Boötes, *XMM*-COSMOS, XRT-SDSS, and XXL-N samples assuming that their L_X–$L_{6\,\mu\mathrm{m}}$ relation follows the bilinear equation

$$\begin{aligned}
&\log L_{6\,\mu\mathrm{m}} < \log L^{\star}_{6\,\mu\mathrm{m}}:\\
&\quad \log L_X = m_1 \times \log \frac{L_{6\,\mu\mathrm{m}}}{10^{45}\ \mathrm{erg\ s^{-1}}} + b_1\\
&\log L_{6\,\mu\mathrm{m}} \geqslant \log L^{\star}_{6\,\mu\mathrm{m}}:\\
&\quad \log L_X = m_2 \times \log \frac{L_{6\,\mu\mathrm{m}}}{10^{45}\ \mathrm{erg\ s^{-1}}} + b_2, \qquad (1)
\end{aligned}$$

discussed by Fiore et al. (2009). Here $L^{\star}_{6\,\mu\mathrm{m}}$ is the "breaking luminosity," and (m_1, b_1) and (m_2, b_2) stand for the slope and intercept for each segment of the bilinear relation, respectively. This equation is identical to the assumption that L_X and $L_{6\,\mu\mathrm{m}}$ follow a broken power-law relation in the linear space. Since the broken power-law relation assumes continuity on the breaking point, the number of free parameters is 3, because $b_2 = \log L^{\star}_{6\,\mu\mathrm{m}} \times (m_1 - m_2) + b_1$. We next fit the data using an iterative χ^2 minimization algorithm (Levenberg–Marquardt) based on the MPFIT package in IDL. The best-fitting parameters for ($\log L^{\star}_{6\,\mu\mathrm{m}}$, m_1, m_2, b_1, b_2) are (44.79, 0.84, 0.40, 44.60, 44.51), and the corresponding uncertainties are (0.11, 0.03, 0.03, 0.01, 0.01). We show this best-fit broken power-law relation in Figure 3. The break luminosity of our bilinear relation is significantly higher than that found by Fiore et al. (2009). This is not surprising, as there are very few objects in the Fiore et al. (2009) sample with mid-IR luminosity smaller than their break luminosity. For our combined sample of X-ray-detected type 1 AGNs, there are 1301 sources with $L_{6\,\mu\mathrm{m}}$ smaller than our best-fit break luminosity,

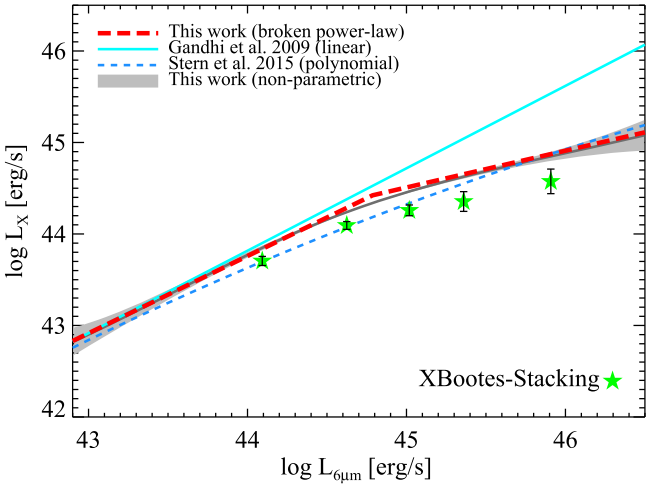

Figure 3. Updated L_X–$L_{6\,\mu m}$ relations derived using the X-ray-detected type 1 AGNs studied in this work. The updated relation is best described by a broken power law (red, thick dashed line). At high 6 μm luminosities, our result is more consistent with the Fiore et al. (2009) and Stern (2015) luminosity-dependent L_X–$L_{6\,\mu m}$ relations than the Gandhi et al. (2009) linear relation. The nonparametric fit to the X-ray-detected sources is also shown as the dark-gray line with the 1σ uncertainty indicated by the shaded region. We also include the XBoötes X-ray stacking results to show the effect of X-ray nondetections (green stars).

$L_{6\,\mu m} = 6.2 \times 10^{44}$ erg s^{-1}. We also fit the data with a simple linear relation, $\log L_X = \alpha \times \log(L_{6\,\mu m}/10^{45}\,\mathrm{erg\,s^{-1}}) + \beta$, and an F-test rejects this model over the bilinear model with a >99.9% confidence level according to the F-test probability. It is also important to note that the location of the break luminosity might depend strongly on how the sample populates the L_X–$L_{6\,\mu m}$ parameter space. To assess how the sparse distribution of our sample in L_X–$L_{6\,\mu m}$ affects the results, we divide our sample into six $L_{6\,\mu m}$ bins of approximately equal size. We then weight the total χ^2 of each bin by its source number such that $L_{6\,\mu m}$ bins with smaller source numbers have similar statistical power to the $L_{6\,\mu m}$ bins with larger source numbers. We find that the break luminosity increases by 0.5 dex with this approach.

In practice, the result of fitting a bilinear L_X–$L_{6\,\mu m}$ relation to an unevenly distributed AGN sample will depend on not only the intrinsic L_X–$L_{6\,\mu m}$ slopes but also the relative numbers of low-luminosity AGNs and luminous quasars. Due to the volume and flux-limited nature of extragalactic surveys, it is extremely difficult to construct a sample that could populate the L_X–$L_{6\,\mu m}$ parameter space as evenly as our simple weighted χ^2 minimization exercise effectively does. Therefore, we consider the result of this simple exercise an "upper limit" on the break luminosity of a bilinear L_X–$L_{6\,\mu m}$ relation and conclude that the linear L_X–$L_{6\,\mu m}$ relation for lower-luminosity AGNs cannot be extended to quasars that are more luminous than $L_{6\,\mu m} = 1.4 \times 10^{45}$ erg s^{-1}.

In Figure 3, we compare our bilinear regression fit with the Gandhi et al. (2009) linear relation for local Seyferts and the second-order polynomial fit of Stern (2015). While our bilinear relation is largely consistent with the second-order polynomial fit of Stern (2015), it is not clear which regression model is the best option. Therefore, in addition to assuming that the L_X–$L_{6\,\mu m}$ distribution follows a specific functional form, it is also useful to adopt a nonparametric approach to visualize the relation between L_X and $L_{6\,\mu m}$ of our sample.

We use the Gaussian process regression algorithm from GPy[18] with a polynomial kernel function to fit all of the X-ray-detected sources studied in this work. The Gaussian process regression algorithm assumes that the dependent variable (the L_X in this work) of a sample of finite size could be described by a multivariate Gaussian function with dimensions equal to the sample size. With an assumed kernel function (i.e., the covariance function of the Gaussian process), the Gaussian process algorithm also takes the measurement uncertainties into account and analytically finds the best-fit multivariate Gaussian function. We can then compute the nonparametric prediction using the posterior probability function based on the Gaussian process regression results.

In Figure 3, we also show this nonparametric fit to the data with 1σ uncertainty as the gray shaded region. We find that both our bilinear regression fit and the second-order polynomial fit of Stern (2015) follow the nonparametric prediction closely, which demonstrates that a change of the L_X–$L_{6\,\mu m}$ slope occurs at $L_{6\,\mu m} \sim 10^{44}$–$10^{45}$ erg s^{-1}.

5. Possible Biases and Comparison to the Literature

In this section, we explore how the different observational constraints affect the estimate of the intrinsic L_X–$L_{6\,\mu m}$ relation for AGNs. For simplicity, we do not consider the broken power-law regression when addressing various observational constraints. Instead, we focus on how X-ray absorption, X-ray nondetections, and X-ray flux limits affect the linear L_X–$L_{6\,\mu m}$ relation of the more luminous objects in our sample (i.e., the quasars with $\log L_{6\,\mu m}/\,\mathrm{erg\,s^{-1}} > 43.8$, which corresponds to a bolometric luminosity of 10^{45} erg s^{-1} assuming the Hopkins et al. [2007] bolometric correction factors).

5.1. Accounting for X-Ray-nondetected Type 1 Quasars

For the shallow flux limits of the Boötes and XRT-SDSS samples, a significant fraction of sources are not detected in the X-rays. For the Boötes type 1 AGNs, Hickox et al. (2007) used an X-ray stacking analysis to show that the X-ray properties of the X-ray-undetected type 1 mid-IR quasars are consistent with luminous X-ray AGNs with little or no absorption. Therefore, it is important to take into account the average X-ray contribution for those optically unobscured quasars without a direct X-ray detection when deriving the L_X–$L_{6\,\mu m}$ correlation since their average X-ray luminosity could be non-negligible.

For the Boötes quasars, we used an X-ray stacking analysis to account for sources not individually detected in X-rays. We divide these quasars into five bins of $L_{6\,\mu m}$ and calculated their stacked X-ray luminosity. We define the stacked X-ray counts as the average number of background-subtracted photons detected within the 90% point-spread function (PSF) energy encircled radius at 1.5 keV, r_{90}, where $r_{90} = 1'' + 10''(\theta/10')^2$ and θ is the angle from the *Chandra* optical axis.[19] We only include sources within $\theta < 6'$ ($r_{90} < 4.''6$) in the analysis. We adopt background surface brightnesses of 3.0 and 5.0 counts s^{-1} deg^{-2} for the 0.5–2 keV and 2–7 keV bands, respectively, based on the estimates of the diffuse background from Hickox et al. (2007). We convert count rates (counts s^{-1}) to flux (erg cm^{-2} s^{-1}) using the conversion factors 6.0×10^{-12} erg cm^{-2} count^{-1} in the 0.5–2 keV band and 1.9×10^{-11} erg cm^{-2} count^{-1} in the

[18] http://sheffieldml.github.io/GPy/

[19] *Chandra* Proposers' Observatory Guide (POG), available at http://cxc.harvard.edu/proposer/POG.

2–7 keV band. To estimate the average X-ray stacking luminosity from the X-ray flux, we assume that all galaxies in each bin of $L_{6\,\mu\mathrm{m}}$ reside at the average luminosity distance for the galaxies in that bin. More details of the stacking procedure are described in Section 5.1 of Hickox et al. (2007).

To derive the L_X–$L_{6\,\mu\mathrm{m}}$ relation including both the X-ray-detected and X-ray-nondetected sources, we calculate the average L_X in bins of $L_{6\,\mu\mathrm{m}}$ by taking the weighted average of the individually detected sources and the stacking luminosity. We find that the average L_X of the entire Boötes sample has an $L_X - L_{6\,\mu\mathrm{m}}$ slope similar to that of the X-ray-detected sources derived in Section 4 (also see Figure 3) with a smaller intercept: $\log L_X = (0.51 \pm 0.06) \times \log L_{6\,\mu\mathrm{m}}/10^{45}\,\mathrm{erg\,s^{-1}} + (44.23 \pm 0.05)$.

Another useful approach to take the X-ray-nondetected sources into account when deriving the linear relation between L_X and $L_{6\,\mu\mathrm{m}}$ is the Bayesian maximum likelihood method presented by Kelly (2007, hereafter K07). The K07 method determines the best-fit linear relation by sampling the L_X values of nondetected sources from the prior provided by the detected sources and the value of the upper limits. For the Boötes and the XRT-SDSS samples, the L_X upper limits for the X-ray-nondetected sources were calculated using the flux limits and the corresponding redshift for each source. We then use the K07 method to recalculate the best-fitting parameters for the complete Boötes and XRT-SDSS samples, respectively. In detail, we use K07's method to perform Markov chain Monte Carlo simulation using a Metropolis–Hastings algorithm sampler with 10,000 iterations to obtain the posterior probability distribution of the linear regression parameters. The best-fitting parameters are determined as the median of the posterior probability distributions of the model parameters. We adopt the 1σ (68%) uncertainties as the 16th and 84th percentiles of the posterior probability distributions.

In the first part of Table 2, we list the best-fitting parameters for different samples with and without the consideration of X-ray nondetections calculated using the K07 method. For comparison, we also list the best-fit minimum χ^2 regression result for the data from the Boötes stacking analysis. We also list the best-fit parameters for the *XMM*-COSMOS and XXL-N samples calculated using the K07 method. For the XRT-SDSS sample, due to the luminous nature of the SDSS DR5 catalog and the 10 ks X-ray exposure time cut, the X-ray detection fraction is >83%. This leads to a similar L_X–$L_{6\,\mu\mathrm{m}}$ relation regardless of the treatment of the X-ray nondetections. For the Boötes sample, we find that the inclusion of X-ray-nondetected sources does lead to a best fit with a smaller L_X throughout the $L_{6\,\mu\mathrm{m}}$ range. This might be due to Eddington bias, as the XBoötes sources have as few as 4 counts in the 5 ks XBoötes *Chandra* observations. The slopes of the L_X–$L_{6\,\mu\mathrm{m}}$ relation also do not change significantly when compared to the best-fit result for the X-ray-detected sources. The slopes derived from the stacked average are also consistent with the results using the K07 regression analysis on samples with and without the inclusion of X-ray nondetections.

The results suggest that the inclusion of X-ray-nondetected objects does not alter the L_X–$L_{6\,\mu\mathrm{m}}$ relation significantly given the relatively high X-ray detection fraction of the Boötes and *Swift*/SDSS samples.

5.2. Effects of X-Ray Absorption on L_X–$L_{6\,\mu\mathrm{m}}$

As we mentioned at the end of Section 3.1, a large fraction of our type 1 quasars do not have sufficient X-ray photon counts to properly correct for attenuation of the observed L_X owing to the small gas absorption. The recent study of L_X–$L_{6\,\mu\mathrm{m}}$ (Stern 2015) using the type 1 quasars from Just et al. (2007) also assumed that type 1 quasars have negligible X-ray absorption column densities. While the average hardness ratio for type 1 AGNs does support this assumption (Hickox et al. 2007), a recent study by Merloni et al. (2014) that also focused on the XMM-COSMOS type 1 AGNs has also shown that a non-negligible fraction (∼20%) of optical type 1 AGNs have a hardness ratio consistent with $N_H > 10^{22}\,\mathrm{cm^{-2}}$ (see Figure 4 of Merloni et al. 2014).

Although the effect of absorption is less significant for high-redshift quasars because the observed X-rays correspond to harder rest-frame energies, it is still important to understand the impact of gas absorption on the observed L_X–$L_{6\,\mu\mathrm{m}}$ relation. We estimate the effect of the bias caused by the possible presence of X-ray obscuration by conservatively assuming that 20% of the sources have $N_H = 10^{23}\,\mathrm{cm^{-2}}$. We note that this assumption is an extreme case in which many of the optical type 1 AGNs are heavily obscured in the X-ray. For the *XMM*-COSMOS sample studied by Merloni et al. (2014), less than 5% of the optical type 1 AGNs have hardness ratios consistent with $N_H > 10^{23}\,\mathrm{cm^{-2}}$. We estimate the correction on the L_X–$L_{6\,\mu\mathrm{m}}$ relations using the following steps: (1) Randomly select 20% of the X-ray-detected sources. (2) Assume that these objects have an absorption column density of $N_H = 10^{23}\,\mathrm{cm^{-2}}$, and calculate the "de-absorbed" X-ray luminosity with an intrinsic X-ray spectral index of $\Gamma = 1.8$. (3) Recalculate the best-fit L_X–$L_{6\,\mu\mathrm{m}}$ relations using the de-absorbed X-ray luminosities and the K07 method. (4) Repeat steps 1–3 1000 times. The result of this bootstrapping analysis suggests that even for the unlikely case in which 20% of the optical type 1 AGNs have heavy absorbing column densities, the slope of L_X–$L_{6\,\mu\mathrm{m}}$ is only ≈0.01 lower than the result neglecting absorption. The median values and standard deviations of the slopes and intercepts from the bootstrapping analysis are listed in Table 2.

A larger part of this is that Compton-thin absorption has little effect on X-ray luminosity estimates for higher-redshift sources (see, e.g., Just et al. 2007; Stern 2015). At $z \sim 1$, even for an AGN obscured by $N_H \sim 10^{23}\,\mathrm{cm^{-2}}$ column densities, its observed-frame 0.5–7 keV flux would only be attenuated by ∼50%. Therefore, it is not surprising that the L_X–L_{MIR} relation does not change significantly even for the case in which 20% of the type 1 AGNs are X-ray absorbed. Since gas absorption only has a small effect on the slope of the L_X–L_{MIR} relation, the difference between the flattened L_X–$L_{6\,\mu\mathrm{m}}$ relation found in our study (and Fiore et al. 2009; Stern 2015) and the linear relation that extends to luminous AGNs reported by Mateos et al. (2015) and Asmus et al. (2015) must be caused by factors other than the possible presence of absorption in optical type 1 AGNs.

5.3. Effects of X-Ray Flux Limits

As we have shown in Section 5.1, the exclusion of X-ray-nondetected sources could result in a biased L_X–$L_{6\,\mu\mathrm{m}}$ relation, but the effect is within the uncertainty for the Boötes and XRT-SDSS samples owing to their high X-ray detection fractions. In Section 5.2, we also show that X-ray absorption should have little effect on the L_X–$L_{6\,\mu\mathrm{m}}$ relation for luminous quasars. Here we examine whether the X-ray flux limits are the primary factor that drives the various L_X–$L_{6\,\mu\mathrm{m}}$ relations reported in the

Table 2
Best-fit Parameters for $L_X = \alpha \times L_{6\,\mu m} + \beta$ Calculated Using the Kelly (2007) Method

Sample (1)	Description (2)	N_{XD} (3)	N_{UL} (4)	α (5)	β (6)
I. Best-fit Parameters for Luminous Quasars (See Section 5.1)					
Boötes[a]	Stacking	727	620[b]	0.51 ± 0.06	44.23 ± 0.05
Boötes	X-ray detected	727	0	0.50 ± 0.02	44.36 ± 0.01
Boötes	All	727	620	0.49 ± 0.03	44.02 ± 0.02
XMM-COSMOS	All, X-ray selected	293	0	0.51 ± 0.03	44.30 ± 0.02
Swift/SDSS (10 ks)	X-ray detected	198	0	0.56 ± 0.05	44.31 ± 0.03
Swift/SDSS (10 ks)	All	198	43	$0.56^{+0.05}_{-0.06}$	44.24 ± 0.03
Swift/SDSS (5 ks)	X-ray detected	247	0	$0.58^{+0.05}_{-0.04}$	44.40 ± 0.03
Swift/SDSS (5 ks)	All	247	115	0.58 ± 0.05	44.24 ± 0.03
XMM-XXL-N	X-ray selected	1071	0	0.59 ± 0.02	44.36 ± 0.01
II. Effects of X-Ray Absorption (see Section 5.2)					
Boötes (X-ray detected)	Assuming that 20% of the sample is X-ray obscured	727	0	0.49 ± 0.05	44.41 ± 0.01
III. Effects of X-Ray Flux Limit (see Section 5.3)					
Mateos et al. 2015	Type 1 AGNs with $L_{6\,\mu m} > 10^{43.8}$ erg s^{-1}	103	0	0.81 ± 0.06	44.58 ± 0.04
Boötes (X-ray detected)	$f_X > 1.0 \times 10^{-13}$ (erg s^{-1}) (M15)	31	0	$0.80^{+0.11}_{-0.12}$	44.59 ± 0.07
Boötes (X-ray detected)	$f_X > 5 \times 10^{-14}$ (erg s^{-1}) (W12 5ks)	163	0	0.58 ± 0.05	44.45 ± 0.03
Boötes (X-ray detected)	$f_X > 2.5 \times 10^{-14}$ (erg s^{-1}) (W12 10ks)	403	0	0.52 ± 0.03	44.42 ± 0.02
Boötes (X-ray detected)	$f_X > 1.1 \times 10^{-14}$ (erg s^{-1}) (XXL-N)	665	0	0.51 ± 0.02	44.38 ± 0.01

Notes. Columns: (1) Sample. (2) Description. (3) Number of X-ray-detected quasars. (4) Number of quasars with only an L_X upper limit. (5) Slope of the best-fit L_X–$L_{6\,\mu m}$ relation. (6) Intercept of the best-fit L_X–$L_{6\,\mu m}$ relation in log erg s^{-1}. Part I: the best-fit parameters for different samples. See Section 5.1 for a complete discussion. Part II: the median value of the best-fit parameters between the intrinsic L_X and $L_{6\,\mu m}$ assuming that 20% of the Boötes sample is heavily X-ray obscured. We show that the parameters do not change significantly. See Section 5.2 for details. Part III: the best-fit parameters of the Boötes subsamples selected with different flux limits. See Section 5.3 for a complete discussion.
[a] Best-fit parameters for the Boötes stacking results are derived using a simple χ^2 minimization method; see Section 5.1.
[b] The number of stacked sources.

literature. We note that the mid-IR survey flux limits for luminous quasars are more homogeneous across different studies than the X-ray flux limits, as almost every luminous optical quasar in studies of the L_X–$L_{6\,\mu m}$ relation has clear detections at mid-IR wavelengths.

Recently, Mateos et al. (2015, hereafter M15) reported an L_X–$L_{6\,\mu m}$ relation for the hard X-ray (4.5–10 keV) sample selected from the Bright Ultra-hard *XMM-Newton* Survey (BUXS). They found an approximately linear L_X–$L_{6\,\mu m}$ relation even for X-ray-luminous quasars with L_X up to $\approx 10^{46}$ erg s^{-1}, in disagreement with our results and the results from Fiore et al. (2009) and Stern (2015).[20] The M15 sample has a hard (4.5–10 keV) X-ray flux limit of 6×10^{-14} erg s^{-1}cm^{-2}. To convert the flux limit to an energy range comparable to the 0.5–7 keV of the *Chandra* observations, we assume a simple power-law X-ray spectrum with a photon index $\Gamma = 1.8$. Thus, the flux limit for the BUXS is equivalent to $\sim 1.6 \times 10^{-13}$ erg s^{-1} cm^{-2} at 0.5–7 keV, which is approximately 2 dex shallower than the *XMM*-COSMOS sample and 1 dex shallower than the Boötes and the XRT-SDSS samples.

[20] M15 fitted the SEDs of their sources with separate AGN accretion disk and AGN torus components. Thus, the $L_{6\,\mu m}$ in M15 is inevitably lower than the $L_{6\,\mu m}$ of our work, which is derived by decomposing the AGN and host galaxy components instead of separating the AGN accretion disk and AGN torus components. However, we note that the difference is small as the typical AGN accretion disk contribution is very small at 6 μm ($\sim$9%, according to M15). In this work, we compare the L_X–$L_{6\,\mu m}$ relation from M15 with our results by adding the average 9% AGN accretion disk emission back to the $L_{6\,\mu m}$ reported in that work.

To test whether the different slope observed in M15 is due to the shallow X-ray flux limit, we apply several different X-ray flux limits to the Boötes sample and examine their effect on the slope of the derived L_X–$L_{6\,\mu m}$ relation. We first apply the XRT-SDSS 10 and 5 ks flux limits and the XXL-N flux limit to the Boötes sample, and we find that the $L_X/L_{6\,\mu m}$ slopes for the Boötes sample decrease for lower flux limits.

We next apply the converted BUXS flux limits to the Boötes sample and recalculate the L_X–$L_{6\,\mu m}$ relation using the K07 method. Due to the shallowness of the BUXS flux limit, there are only 38 sources in Boötes with an X-ray flux larger than 1×10^{-13} erg s^{-1}cm^{-2}. Considering the difference in survey area, the number of sources is consistent with the M15 type 1 sample. For the Boötes type 1 AGNs, only 4% of the sources would have a flux limit higher than that of the M15 sample, suggesting that surveys with shallow X-ray flux limits will produce a biased L_X–$L_{6\,\mu m}$ relation because they miss the vast majority of the AGN population of similar L_{MIR}.

The best-fit L_X–$L_{6\,\mu m}$ slope estimated using the K07 method for the Boötes subsample with the 1×10^{-13} erg s^{-1}cm^{-2} cut is significantly steeper than the original Boötes sample. This highlights the necessity of deep X-ray observations in order to reveal the intrinsic L_X–$L_{6\,\mu m}$ relation when the X-ray survey flux limits are too shallow. Figure 4 shows the effect of survey X-ray flux limits on the slope of the L_X–$L_{6\,\mu m}$ relation.

It is also interesting that the best-fit slope for the XXL-N sample is 0.59 ± 0.02, which is higher than that of the X-ray-detected AGNs in Boötes, 0.50 ± 0.02, despite their similar X-ray flux limits. This is likely due to the fact that XXL-N has

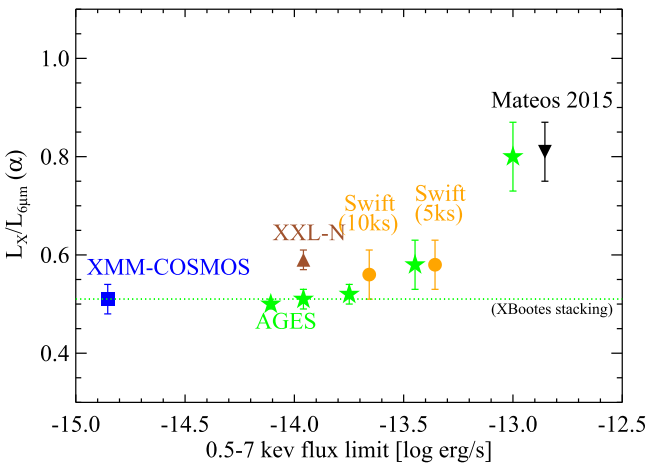

Figure 4. Dependence of the slope of the L_X–$L_{6\,\mu m}$ relation on the effective X-ray flux limit. The green stars are the $L_X/L_{6\,\mu m}$ slopes for X-ray-detected subsamples from AGES selected with different X-ray flux limits. For comparison, the M15 and XRT-SDSS samples from which the X-ray flux limits are drawn are also plotted as the downward-pointing triangle (M15) and the orange circles (XRT-SDSS). The *XMM*-COSMOS sample is shown as the blue square. We note that all of the $L_X/L_{6\,\mu m}$ slopes are derived for the luminous ($L_{6\,\mu m} > 10^{43.8}$ erg s^{-1}) quasars using the K07 method.

more extremely luminous sources owing to its larger survey volume. It is also possible that a small number of high-redshift radio-loud quasars in XXL-N were not identified in the shallow VLA FIRST catalog (∼1 mJy). Nonetheless, the best-fit L_X–$L_{6\,\mu m}$ slopes for the four samples studied in this work are still much smaller than the results reported in previous studies with much shallower flux limits, suggesting that the intrinsic L_X–L_{MIR} relation could only be recovered by considering samples selected from both deep and wide X-ray surveys.

5.4. Host Galaxy Contamination at Mid-IR Wavelengths

In contrast to X-ray flux limits that might cause a steeper $L_X/L_{6\,\mu m}$ relation, contamination from host galaxies at mid-IR wavelengths could cause the observed $L_X/L_{6\,\mu m}$ relation to be shallower than its intrinsic value (e.g., Lusso et al. 2013).

We have carefully modeled the possible cool dust contamination using the strong constraints provided by *Herschel* observations at far-IR wavelengths. Here we further scrutinize the SEDs for the X-ray-nondetected, mid-IR bright type 1 quasars in our Boötes and *XMM*-COSMOS samples. We find that they have a median AGN fraction of 88% at rest-frame 6 μm, suggesting that their mid-IR SEDs are almost entirely dominated by the AGN component. For the high-$L_{6\,\mu m}$ sources in our sample, the W3 and MIPS 24 μm bands still show no signs of strong PAH emission or silicon absorption. While it is possible for strong nuclear starbursts to produce mid-IR continuum with spectra similar to those of the AGN template (e.g., Ballantyne 2008), local nuclear starburst galaxies are often hosted by less massive galaxies with moderate-luminosity AGNs with L_X less than the average L_X of our mid-IR-bright quasars. In Section 3.2 we also demonstrated that the host galaxy contamination is small even for far-IR-luminous objects in Boötes and *XMM-Newton*. Thus, we argue that for our sample of luminous quasars, it is unlikely that the high $L_{6\,\mu m}$ derived from the best-fitting AGN template is due to substantial contamination from their host galaxies. Since the mid-IR luminosity in our type 1 quasars is indeed powered by the AGN, the shallower L_X–$L_{6\,\mu m}$ slope suggests that the AGN X-ray luminosity does not trace the AGN mid-IR luminosity in the same fashion as seen in local Seyfert galaxies.

6. Discussion and Conclusion

In this paper, we study the possible origins of the disparity between the different L_X–$L_{6\,\mu m}$ relations found in the literature. We assemble samples of spectroscopically confirmed broad-line AGNs (type 1) across a wide range of X-ray survey areas and depths to investigate the AGN intrinsic L_X–$L_{6\,\mu m}$ relation for luminous quasars. We test several observational constraints that could bias the observed L_X–$L_{6\,\mu m}$ relation, including intrinsic X-ray absorption, host galaxy contamination at mid-IR wavelengths, and X-ray survey flux limit. We argue that the most important factor that differentiates the L_X–$L_{6\,\mu m}$ relations from different studies is the X-ray survey flux limits (i.e., the Eddington bias), as we find that other factors do not affect the L_X–$L_{6\,\mu m}$ relation of luminous quasars significantly.

For the 2509 X-ray-detected AGNs in our sample, we find that their L_X–$L_{6\,\mu m}$ relation could be well described by the bilinear function

$$\begin{aligned}
&\log L_{6\,\mu m}/\mathrm{erg\ s^{-1}} < 44.63:\\
&\log \frac{L_X}{\mathrm{erg\ s^{-1}}} = (0.84 \pm 0.03)\log \frac{L_{6\,\mu m}}{10^{45}\mathrm{erg\ s^{-1}}} + 44.58 \pm 0.01\\
&\log L_{6\,\mu m}/\mathrm{erg\ s^{-1}} \geqslant 44.63:\\
&\log \frac{L_X}{\mathrm{erg\ s^{-1}}} = (0.54 \pm 0.03)\log \frac{L_{6\,\mu m}}{10^{45}\mathrm{erg\ s^{-1}}}\\
&\quad + 44.47 \pm 0.01,
\end{aligned} \tag{2}$$

where the break luminosity is $\log L_{6\,\mu m}/\mathrm{erg\ s^{-1}} \approx 44.63 \pm 0.11$. For luminous quasars, the slope of their L_X–$L_{6\,\mu m}$ relation is significantly flatter than the approximately linear relation observed in low- to moderate-luminosity AGNs (Gandhi et al. 2009; Asmus et al. 2015), which supports studies that suggest that type 1 quasars have higher L_{MIR}-to-L_X ratios than their local Seyfert counterparts (Fiore et al. 2009; Stern 2015).

The fit in Equation (2) does not take the X-ray-nondetected AGNs into account, but we also show that the inclusion of X-ray-nondetected AGNs does not affect the L_X–$L_{6\,\mu m}$ slope significantly given the high X-ray detection fractions of our samples.

Since the rest-frame mid-IR emission in AGNs originates from hot dust heated by UV photons from the accretion disk, it is natural to consider the well-studied ratio between X-ray and UV monochromatic luminosities ($\alpha_{ox} = 0.38(\log L_{2\,\mathrm{keV}}/L_{2500\,\text{Å}})$) to explain the luminosity-dependent L_X–$L_{6\,\mu m}$ relation. As pointed out by a number of studies (e.g., Tananbaum et al. 1979; Strateva et al. 2005), the relation of α_{OX} to AGN UV luminosity suggests that UV-luminous AGNs have relatively weak X-ray emission compared to their less luminous counterparts. On the other hand, the radiation mechanism of AGN rest-frame mid-IR emission is driven by the UV photons from the accretion disk and the geometry of the dusty torus itself. While several dusty torus models and observations have described the effect of increasing AGN UV luminosity on the geometry of the dust distribution (Lawrence 1991; Lusso et al. 2013), these models only predict a luminosity-dependent AGN obscured fraction, and no drastic change of AGN UV to mid-IR spectral shapes is suggested. In fact, observational studies by Treister et al. (2008) and Lusso et al.

(2010) have shown that the ratio of AGN mid-IR to bolometric luminosity is only weakly dependent on the AGN bolometric luminosity. Studies of average SDSS quasar SEDs with different infrared luminosities have also found marginal variation in the average UV to mid-IR SEDs (Richards et al. 2006; Assef et al. 2011).

The relatively weak X-ray emission in luminous quasars has also been found in studies of X-ray bolometric corrections (e.g., Hopkins et al. 2007; Vasudevan & Fabian 2007; Lusso et al. 2013), which suggest that X-ray bolometric correction factors increase for AGNs with higher accretion efficiency (i.e., with higher Eddington rates). The increase of X-ray bolometric correction factor in luminous quasars has also been implicitly suggested by the luminosity-dependent density evolution of the AGN X-ray luminosity function (Aird et al. 2010), as the rapid drop of the X-ray luminosity function implies that the most luminous X-ray AGNs are extremely rare. On the other hand, the AGN mid-IR luminosity function does not drop as significantly (e.g., Brown et al. 2006).

If AGN X-ray and mid-IR luminosities followed the tight L_X–$L_{6\,\mu m}$ correlation seen in the local Seyfert galaxies, there would be as many as 40 type 1 quasars with $L_X > 10^{44.7}$ erg s^{-1} in the survey volume of XBoötes. However, according to the recent Aird et al. (2010) X-ray luminosity function measured using deep X-ray surveys, the number of AGNs with $L_X > 10^{44.7}$ erg s^{-1} should only be 22.3 in the volume and redshift range of the Boötes data set used in this work. In Boötes, there are only 18 sources more luminous than $L_X > 10^{44.7}$ erg s^{-1}. Indeed, recent discoveries of the most infrared luminous AGNs in the universe, the hot dust-obscured galaxies (hot-DOGs; e.g., Eisenhardt et al. 2012; Wu et al. 2012b; Tsai et al. 2015), have also found that their intrinsic X-ray luminosity is more consistent with the luminosity-dependent L_X–$L_{6\,\mu m}$ relations (Stern et al. 2014; Assef et al. 2016; Ricci et al. 2016).

In conclusion, we have shown that for type 1 quasars, the relationship between AGN mid-IR and X-ray luminosities is not a simple power law, as has been observed for nearby Seyfert-luminosity AGNs. This result is crucial for the studies of AGN–galaxy coevolution, as the dynamical range of X-ray luminosities is considerably smaller than the dynamical range of AGN mid-IR luminosities.

Much of this work was in progress at the time of Steve Murray's untimely death in 2015. This work would not have been possible without his generous GTO contribution to the XBoötes data set and his strong support of Boötes multi-wavelength surveys. He will be greatly missed by all of us. We thank the referee for a careful reading and constructive suggestions that have improved the manuscript. C.-T.J.C. was supported by the William H. Neukom 1964 Institute for Computational Science. R.C.H. acknowledges support from the National Science Foundation through AST award no. 1515364 and from an Alfred P. Sloan Research Fellowship. R.J.A. was supported by FONDECYT grant no. 1151408. This publication makes use of data products from the *Wide-field Infrared Survey Explorer*, which is a joint project of the University of California, Los Angeles, and the Jet Propulsion Laboratory/California Institute of Technology, funded by the National Aeronautics and Space Administration. This publication also makes use of data products from the Two Micron All Sky Survey, which is a joint project of the University of Massachusetts and the Infrared Processing and Analysis Center/California Institute of Technology, funded by the National Aeronautics and Space Administration and the National Science Foundation. Funding for SDSS-III has been provided by the Alfred P. Sloan Foundation, the Participating Institutions, the National Science Foundation, and the U.S. Department of Energy Office of Science. The SDSS-III Web site is http://www.sdss3.org/.

References

Adelman-McCarthy, J. K., Agüeros, M. A., Allam, S. S., et al. 2007, ApJS, 172, 634
Aird, J., Nandra, K., Laird, E. S., et al. 2010, MNRAS, 401, 2531
Alberts, S., Pope, A., Brodwin, M., et al. 2013, MNRAS, 431, 194
Alexander, D. M., Chary, R. R., Pope, A., et al. 2008, ApJ, 687, 835
Ashby, M. L. N., Stern, D., Brodwin, M., et al. 2009, ApJ, 701, 428
Asmus, D., Gandhi, P., Hönig, S. F., Smette, A., & Duschl, W. J. 2015, MNRAS, 454, 766
Asmus, D., Honig, S. F., Gandhi, P., Smette, A., & Duschl, W. J. 2014, MNRAS, 439, 1648
Assef, R. J., Kochanek, C. S., Ashby, M. L. N., et al. 2011, ApJ, 728, 56
Assef, R. J., Kochanek, C. S., Brodwin, M., et al. 2010, ApJ, 713, 970
Assef, R. J., Walton, D. J., Brightman, M., et al. 2016, ApJ, 819, 111
Ballantyne, D. R. 2008, ApJ, 685, 787
Becker, R., White, R., & Helfand, D. 1995, ApJ, 450, 559
Brinkmann, W., Laurent-Muehleisen, S. A., Voges, W., et al. 2000, A&A, 462, 445
Brown, M. J. I., Brand, K., Dey, A., et al. 2006, ApJ, 638, 88
Brown, M. J. I., Dey, A., Jannuzi, B. T., et al. 2007, ApJ, 654, 858
Brusa, M., Civano, F., Comastri, A., et al. 2010, ApJ, 716, 348
Buchner, J., Georgakakis, A., Nandra, K., et al. 2014, A&A, 564, A125
Burrows, D. N., Hill, J. E., Nousek, J. A., et al. 2005, SSRv, 120, 165
Capak, P., Aussel, H., Ajiki, M., et al. 2007, ApJS, 172, 99
Cappelluti, N., Brusa, M., Hasinger, G., et al. 2009, A&A, 497, 635
Cappi, M., Matsuoka, M., Comastri, A., et al. 1996, ApJ, 478, 492
Cardelli, J. A., Clayton, G. C., & Mathis, J. S. 1989, ApJ, 345, 245
Chary, R., & Elbaz, D. 2001, ApJ, 556, 562
Chen, C.-T. J., Hickox, R. C., Alberts, S., et al. 2015, ApJ, 802, 50
Chung, S. M., Kochanek, C. S., Assef, R., et al. 2014, ApJ, 790, 54
Corrales, L. R., García, J., Wilms, J., & Baganoff, F. 2016, MNRAS, 458, 1345
Dale, D. A., & Helou, G. 2002, ApJ, 576, 159
de Vries, W. H., Morganti, R., Röttgering, H. J. A., et al. 2002, AJ, 123, 1784
Di Matteo, T., Springel, V., & Hernquist, L. 2005, Natur, 433, 604
Eisenhardt, P. R. M., Wu, J., Tsai, C.-W., et al. 2012, ApJ, 755, 173
Elvis, M., Hao, H., Civano, F., et al. 2012, AJ, 759, 6
Fiore, F., Puccetti, S., Brusa, M., et al. 2009, ApJ, 693, 447
Gandhi, P., Horst, H., Smette, A., et al. 2009, A&A, 502, 457
Gehrels, N. 1986, ApJ, 303, 336
Georgakakis, A., & Nandra, K. 2011, MNRAS, 414, 992
Gilli, R., Comastri, A., & Hasinger, G. 2007, A&A, 463, 79
Gonzalez, A. H., Brodwin, M., Brown, M. J. I., et al. 2010, AAS Meeting Abstracts, #216, 415.13
Gordon, K. D., & Clayton, G. C. 1998, ApJ, 500, 816
Goulding, A. D., Alexander, D. M., Mullaney, J. R., et al. 2011, MNRAS, 411, 1231
Hickox, R. C., Jones, C., Forman, W. R., et al. 2007, ApJ, 671, 1365
Hickox, R. C., Jones, C., Forman, W. R., et al. 2009, ApJ, 696, 891
Hopkins, P. F., Hernquist, L., Cox, T. J., et al. 2006, ApJS, 163, 1
Hopkins, P. F., Richards, G. T., & Hernquist, L. 2007, ApJ, 654, 731
Jannuzi, B., & Dey, A. 1999, in ASP Conf. Ser. 191, Photom Redshifts Detect High Redshift Galaxies, ed. R. Weymann et al. (San Francisco, CA: ASP), 111
Just, D. W., Brandt, W. N., Shemmer, O., et al. 2007, ApJ, 665, 1004
Kellermann, K. I., Sramek, R., Schmidt, M., Shaffer, D. B., & Green, R. 1989, AJ, 98, 1195
Kelly, B. C. 2007, ApJ, 665, 1489
Kenter, A., Murray, S. S., Forman, W. R., et al. 2005, ApJS, 161, 9
Kirkpatrick, A., Pope, A., Alexander, D. M., et al. 2012, ApJ, 759, 139
Kochanek, C. S., Eisenstein, D. J., Cool, R. J., et al. 2012, ApJS, 200, 8
Krumpe, M., Miyaji, T., Brunner, H., et al. 2015, MNRAS, 446, 911
Lawrence, A. 1991, MNRAS, 252, 586
Lilly, S. J., Le Brun, V., Maier, C., et al. 2009, ApJS, 184, 218
Liu, Z., Merloni, A., Georgakakis, A., et al. 2016, MNRAS, 459, 1602
Lusso, E., Comastri, A., Vignali, C., et al. 2010, A&A, 512, A34

Lusso, E., Comastri, A., Vignali, C., et al. 2011, A&A, 534, A110
Lusso, E., Hennawi, J. F., Comastri, A., et al. 2013, ApJ, 777, 33
Lutz, D., Maiolino, R., Spoon, H. W. W., & Moorwood, A. F. M. 2004, A&A, 418, 465
Maiolino, R., Shemmer, O., Imanishi, M., et al. 2007, A&A, 468, 979
Mateos, S., Carrera, F. J., Alonso-Herrero, A., et al. 2015, MNRAS, 449, 1422
Menzel, M. L., Merloni, A., Georgakakis, A., et al. 2016, MNRAS, 457, 110
Merloni, A., Bongiorno, A., Brusa, M., et al. 2014, MNRAS, 437, 3550
Mullaney, J. R., Alexander, D. M., Goulding, A. D., & Hickox, R. C. 2011, MNRAS, 414, 1082
Mullaney, J. R., Pannella, M., Daddi, E., et al. 2012, MNRAS, 419, 95
Murray, S. S., Kenter, A., Forman, W. R., et al. 2005, ApJS, 161, 1
Netzer, H., Lutz, D., Schweitzer, M., et al. 2007, ApJ, 666, 806
Oliver, S. J., Bock, J., Altieri, B., et al. 2012, MNRAS, 424, 1614
Pierre, M., Pacaud, F., Adami, C., et al. 2016, A&A, 592, A1
Ricci, C., Assef, R. J., Stern, D., et al. 2016, arXiv:1609.0480
Richards, G. T., Lacy, M., Storrie-Lombardi, L. J., et al. 2006, ApJS, 166, 470
Rieke, G. H., Young, E. T., Engelbracht, C. W., et al. 2004, ApJS, 154, 25
Sanders, D. B., Salvato, M., Aussel, H., et al. 2007, ApJS, 172, 86
Schneider, D. P., Hall, P. B., Richards, G. T., et al. 2007, AJ, 134, 102
Smee, S. A., Gunn, J. E., Uomoto, A., et al. 2013, AJ, 146, 32
Somerville, R. S., Hopkins, P. F., Cox, T. J., Robertson, B. E., & Hernquist, L. 2008, MNRAS, 391, 481
Stern, D. 2015, ApJ, 807, 129
Stern, D., Lansbury, G. B., Assef, R. J., et al. 2014, ApJ, 794, 102
Strateva, I. V., Brandt, W. N., Schneider, D. P., Vanden Berk, D. G., & Vignali, C. 2005, AJ, 130, 387
Tananbaum, H., Avni, Y., Branduardi, G., et al. 1979, ApJL, 234, L9
Treister, E., Krolik, J. H., & Dullemond, C. 2008, ApJ, 679, 140
Treister, E., Urry, C. M., & Virani, S. 2009, ApJ, 696, 110
Tsai, C.-W., Eisenhardt, P. R. M., Wu, J., et al. 2015, ApJ, 805, 90
Tueller, J., Mushotzky, R., Barthelmy, S., et al. 2008, ApJ, 681, 113
Vasudevan, R. V., & Fabian, A. C. 2007, MNRAS, 381, 1235
Wilkes, B. J., & Elvis, M. 1987, ApJ, 323, 243
Wu, J., Vanden Berk, D., Grupe, D., et al. 2012a, ApJS, 201, 10
Wu, X.-B., Hao, G., Jia, Z., Zhang, Y., & Peng, N. 2012b, ApJ, 144, 49
Zamorani, G., Henry, J. P., Maccacaro, T., et al. 1981, ApJ, 245, 357